Estimating elastic and thermal contributions to lattice strains from operando X-ray diffraction measurements using fast simulations

S. Gaudez, D. Weisz-Patrault, K.A. Abdesselam, H. Gharbi, V. Honkimäki, S. van Petegem, M.V. Upadhyay

Estimating elastic and thermal contributions to lattice strains from *operando* X-ray diffraction measurements using fast simulations

S. Gaudez[1,†], D. Weisz-Patrault[1,**], K. A. Abdesselam[1], H. Gharbi[1], V. Honkimäki[2], S. Van Petegem[3], M.V. Upadhyay[1,*]

[1] Laboratoire de Mécanique des Solides (LMS), École Polytechnique, Institut Polytechnique de Paris, CNRS UMR 7649, 91120 Palaiseau, France
[2] European Synchrotron Research Facility, Grenoble, France
[3] Laboratory for Condensed Matter, PSI Center for Photon Science, Forschungsstrasse 111, 5232 Villigen PSI, Switzerland

† Current address: Laboratory for Condensed Matter, PSI Center for Photon Science, Forschungsstrasse 111, 5232 Villigen PSI, Switzerland

* First corresponding author e-mail: manas.upadhyay@polytechnique.edu
** Second corresponding author e-mail: daniel.weisz-patrault@cnrs.fr

---

Keywords: 3D printing; synchrotron; lattice strain; thermomechanical modelling; direct energy deposition; residual stress

Abstract: Lattice strains obtained from *operando* synchrotron X-ray diffraction measurements during metal additive manufacturing are being increasingly used to estimate temperature evolution during the process. At the minimum, these transient lattice strains have contributions from thermal and elastic strains. Temperature estimates from lattice strains have thus far been extracted assuming that elastic strains are negligible in comparison to thermal strains at high temperatures when the heat source is close to the probed region. However, such an assumption may not only lead to inaccuracies in estimating temperature but also fail to correctly estimate the non-negligible stress evolution occurring at moderate to low temperatures as the heat source moves away. Numerical simulations can be used to predict lattice strains but these predictions are necessarily different from experimental measures.

This work proposes an experimentally corrected numerical approach to improve simulation predictions. It involves first using a recently developed fast numerical thermomechanics model to predict lattice strains. Then, the predicted thermal and elastic strains are corrected using a minimization procedure under the strict constraint that the predicted lattice strains are strictly equal to the measured ones, thus improving the original estimates. This strategy is demonstrated for operando synchrotron X-ray diffraction measurements during directed energy deposition of a thin wall made from 316L stainless steel, which exhibits negligible solid-state phase transformations. Following validation, the corrected thermal and elastic strains are used to estimate temperature and stress evolution and study the difference in temperature and heating/cooling rate prediction caused by neglecting elastic strains.

Dataset link: https://doi.org/10.15151/ESRF-ES-611485530

---

1 Introduction

Metal additive manufacturing (AM) involves complex interactions between a heat source and feedstock. The ensuing temperature amplitudes, gradients, and heating/cooling rates determine the nature of the different non-equilibrium processes occurring during AM, which in turn determine the material microstructure, its properties, and the eventual part performance [1, 2]. In addition, non-negligible stress evolution occurs during the process because of thermal expansion and shrinkage in the vicinity of the heat source where liquid metal cools very quickly and solidifies, which may induce defects such as fracture, buckling, or out-of-tolerance geometry. Thus, arguably, temperature is the most important state variable during any metal AM process. Its accurate measurement is necessary to understand the AM process-microstructure–property-performance relationship and to control it.

Due to the rapid nature of AM, probing temperature in real-time is challenging and only a handful of techniques are capable of providing this information. The most common approach that has been used during both directed energy deposition (DED) and powder-bed fusion type AM processes involves direct measurements using infrared pyrometers and/or cameras [3–7], or photodiode [8]. The main difficulty of such techniques is the calibration of the emissivity, which depends on tem perature, surface roughness and material properties. Bi-chromatic technologies enable to mitigate this disadvantage and

to obtain quantitative results [9, 10]. Similarly, probing stress evolution during AM is very challenging. Indirect total deformation measurements are available using digital image correlation techniques [7]; recent developments using the height digital image correlation approach are able to provide a voxel-based full-field eigenstrain reconstruction of final residual stresses [11]. One could use infrared/photodiode and digital image correlation techniques together to probe the evolution of temperature and stresses. The information obtained is however only from the surface of the samples..

An approach to obtain both temperature and stress evolution from the bulk of the material during AM is to study the transient lattice strains obtained from operando synchrotron X-ray diffraction (XRD) measurements; the reader may consult [12–14] to better understand the scope of such experiments. The main advantages of this approach over infrared techniques include the ability to carry out measurements at a very fine length scale (i.e., distinguish family of grains sharing the same crystallographic orientation) and to directly measure the residual elastic strain after the part cools down to room temperature. However, the main disadvantage of *operando* synchrotron XRD measurements is the well-known nontrivial coupling of all the physical phenomena influencing lattice parameters, e.g., thermal expansion, elastic strains, solid-state phase transformations, etc. In practice, however, the contributions of elastic strains and solid-state phase transformations during AM are neglected and temperature is estimated assuming that the lattice strains only have a significant contribution from thermal strains [15–26]. This approximation may work well at high temperatures (close to the melting point of the material) when the heat source is close to the probed region. However, as the heat source moves away and the temperatures drop, non-negligible stresses are generated, and, depending on the material, solid-state phase transformations may occur. Then, neglecting the contributions of elastic and phase transformation strains to lattice strains may induce significant inaccuracies in temperature estimates and more importantly make it impossible to estimate elastic strains that would lead to obtaining stress evolution during the process. The problem can be simplified by studying single-phase materials or using an experimental setup allowing to probe a nearly strain-free direction or both. For example, in an *operando* synchrotron XRD experiment during laser-based powder bed fusion of a single-phase nickel alloy, it was shown that elastic strains on the top surface normal to the building direction were small and could be ignored to estimate temperature [20].

In parallel, temperature and stresses have been estimated from full-field thermomechanical simulations, typically using the finite element approach with three-dimensional (3D) solid elements [27–33]. However, their applications are limited to simulating single or few layers due to their high consumption of computational resources. To overcome this limitation, a fast numerical model of the entire AM process at the part scale was recently developed [5, 7]. This model solves the thermal and mechanical problem in a decoupled manner and differs from the aforementioned approaches in several aspects. First, the thermal analysis is carried out based on semi-analytical solutions for the temperature field while accounting for the latent heat of fusion [5]. Then, the mechanical problem is solved via the finite element method using shell elements with temperature taken as input from the thermal simulation [7]. This one-way coupled approach provides orders of magnitude computational acceleration compared to full-field thermomechanical simulations (using 3D solid elements) at the part scale.

The aforementioned fast model has been previously validated across various geometries and materials. Infrared pyrometer measurements were employed to validate the model for different geometries in 316L stainless steel [5]. Additionally, temperature and displacement predictions were validated on a 316L thin-wall structure using an infrared camera and digital image correlation techniques [7]. Further validation was also performed for 2507 duplex stainless steel by comparing predicted and measured residual phase fractions [34]. However, it has not yet been validated for its thermomechanical predictions during DED, in particular lattice strains containing contributions from both elastic and thermal strains, which can be made possible using *operando* synchrotron XRD. In this work, as a first step, the model is calibrated and validated against operando lattice strain measurements. It should be noted that additional validations would be particularly beneficial for various DED technologies and materials.

Furthermore, because of modeling assumptions numerical results necessarily do not match perfectly with measurements even after calibration of model parameters (e.g., absorptivity). To better exploit available experimental data beyond the simple model calibration, an in-depth analysis is conducted to provide experimentally informed estimates of both elastic and thermal strains by correcting numerical predictions using experimental data. To do so, the distance between the proposed new strain estimates and the strains computed with the fast numerical simulation is minimized under the constraint that the sum of thermal and elastic strain estimates exactly matches the measured lattice strain. In other words, the experimental data are considered as a "ground truth" to which the numerical results are forced to match using a strict constraint in the minimization procedure. The proposed strategy does not involve using numerical simulations to correct experimental data, which are not altered in any way, but instead consists of correcting numerical predictions to perfectly match the experiment. Therefore, the obtained estimates are not direct measurements of thermal and elastic strains, but they are numerical estimates perfectly consistent with measurements and obtained from a validated numerical simulation. Using the proposed estimates, the impact of neglecting elastic strains on temperature estimates is studied, and

more importantly, stress profiles occurring during the process can be derived.

To demonstrate the potential of the aforementioned experimentally corrected numerical strategy, operando synchrotron XRD during laser-based DED of 316L stainless steel (henceforth called 316L) is performed to obtain the transient and residual lattice strain measurements. Laser DED is performed using a custom-built miniature DED (mini-DED) machine designed for in situ (including operando) synchrotron experiments, first used in [35]. 316L is chosen due to the negligible solid-state phase transformations occurring during DED, as shown in [35]. Following the presentation of material and methods, the results begin with the validation of the simulations. After this validation, a constrained minimization problem is solved to derive thermal and elastic strain esti- mates. Then, the relative gap between the improved and conventionally computed temperature estimates from lattice strains is quantified showing the latter's dependence on temperature, stress, sample geometry, and analyzed direction. Furthermore, significant stresses are estimated in the region where elastic strains are usually considered negligible. Finally, it is demonstrated that there is no trivial way to decouple elastic and thermal strains by only using experimental data without additional information provided by numerical modeling.

2 Materials and methods

2.1 Material and printing strategy

AM of 316L was performed using the laser-based mini-DED machine dedicated to performing *in situ* (including *operando*) synchrotron X-ray experiments; a detailed description of the machine can be found in [35]. The feedstock was a 316L powder (Oerlikon AM, Germany) manufactured via inert gas atomization. The average powder particle size was 58 µm with 10% and 90% quantiles being 44 µm and 82 µm, respectively. The chemical composition of the powder in weight percent is reported in Table 1.

Table 1: Chemical composition of the 316L powder in weight percent.

Fe	Cr	Ni	Mo	Mn	Si	N	Cu	O	P	S	C
Bal.	17.34	12.55	2.34	1.40	0.49	0.08	0.04	0.03	0.1	<0.1	<0.1

100-layered thin-wall shaped samples of size $0.6 \times 100 \times 20$ mm^3 (x, y, z) were additively manufactured with the mini-DED machine using a single-pass-per-layer unidirectional printing strategy. The printing direction (PD) was along y and the building direction (BD) was along z. X-ray diffraction experiments provide thickness-averaged measurements in the (y, z) plane. Consequently, selecting a thin-walled structure is akin to dealing with a two-dimensional structure in terms of heat transfer, as the thermal gradients in the thickness direction are negligible compared to those in the build and print directions. The wall thickness is only 600 µm, which is more than an order of magnitude smaller than the other dimensions of the sample. Furthermore, the convection conditions are symmetrically applied to both faces of the wall. In addition, heat transfer from the metal to the surrounding air is significantly less effective compared to heat conduction through the metal along the build and print directions.

Each wall was printed on a 316L substrate of size $40 \times 140 \times 10$ mm^3, 5 mm away from the edge along the transverse direction (TD) x, and centered along the PD y. The following AM parameters were used: laser power = 105 W, printing speed = 10 mm.s^{-1}, powder flow rate = 7 g.min^{-1}, and a mean layer height of 0.2 mm. The continuous-wave fiber laser, whose axis is inclined at 20° to the vertical direction, has a wavelength of 1.08 µm and a Gaussian intensity distribution. The projected spot size at the manufacturing position is $\sim 460 \times 400$ µm^2. The powder is carried vertically through a circular 1 mm internal diameter nozzle accompanied by an Ar gas flow of 0.05 L/min. In addition, to avoid oxidation during the process Ar gas is used to isolate the melt pool at a flow rate of 5 L/min. A dwell time of 14 s was set between the end of a printed layer and the beginning of the next one; this dwell time is the minimum time required to allow the experimental setup to be ready to print the next layer and for the X-ray detector to prepare for the next series of acquisitions. It also includes acceleration and deceleration times (both set at 1 s) of the stage to reach the printing speed. Thus, a full cycle to print one layer took 24 s (10 s of printing + 14 s of dwell time). AM was performed by keeping the printing head (powder and laser) static and by moving the substrate holder along PD (y) with respect to the mini-DED machine.

2.2 *Operando* Synchrotron XRD experiments during AM

These experiments were conducted at the European Synchrotron Radiation Facility (ESRF, France) on beamline ID31. The mini-DED machine was positioned on the heavy duty micro diffraction instrument (HDMD) available at the beamline. A monochromatic 77 keV ($\lambda = 0.16102$ Åand $\Delta\lambda/\lambda = 3 \times 10^{-3}$) X-ray beam of size 300×300 µm^2 (obtained with slits) was used. A Pilatus 3X CdTe 2M 2D detector located at ∼0.8 m downstream to the sample was used to record the diffraction patterns with an acquisition frequency of 20 Hz. Thus, 200 images were recorded for each printed layer.

With this setup, full Debye-Scherrer rings of the first four hkl reflections of the γ-austenite (FCC) phase of 316L were investigated, i.e., 111, 200, 220, and 311. Sample-to-detector distance, detector tilts, and beam center were calibrated using a CeO_2 powder as a reference. The experimental setup and the coordinate system used are presented in Figure 1a.

For each experiment, the vertical distance (z) between the top of the substrate and the center of the X-ray beam was kept fixed to investigate the material at a fixed height on the wall. Three experiments were conducted to measure at three vertical distances (z): 4 mm (20th layer), 7.4 mm (37th layer), and 11 mm (55th layer). Then, the walls were manufactured up to a total of 100 layers ($\sim$ 20 mm) and diffraction patterns were recorded during the addition of each layer. Since the printing head is kept stationary with respect to the mini-DED machine, the substrate holder is moved down ($-z$) by a layer increment (0.2 mm) after the addition of each layer and before printing the next one. At the same time, to maintain the same vertical distance between the substrate and the X-ray beam, the mini-DED machine is moved up ($+z$) by a layer increment (0.2 mm) using the HDMD instrument. In addition, during the printing of a single layer, to continuously investigate multiple locations ahead of the laser as well as behind it, the mini-DED machine was moved in the direction opposite to the PD using the HDMD at a speed of 4 mm.s^{-1} during deposition of a layer (10 s) (Figure 1b). After the deposition, the machine was moved back to its original position during the dwell time.

During the deposition of a layer, the detector was synchronized to start acquiring images when the laser was turned on and to stop acquiring them when the laser was turned off. At the start of the printing of the layer when the laser was just turned on, the X-ray beam was 20 mm ahead of the laser (Fig. 1b). At the end of the printing of that layer, the X-ray beam was 20 mm behind the laser (Fig. 1b). Therefore, from the point of view of the laser, images were acquired in the range $\pm$20 mm around the laser along PD (y) i.e., along a 40 mm distance (d_{l-X}).

Now, for the sample, images were acquired over a length of 60 mm at $\pm$30 mm along y from the center of the sample during a period of 10 s; substrate holder speed ($v_{\text{substrate}}$) of 10 mm.s^{-1} along $-y$ and HDMD speed of 4 mm.s^{-1} along y result in a relative speed of 6 mm.s^{-1} of the X-ray beam with respect to the sample, which requires 10 s to cover the distance of 60 mm. Since 200 images are taken using a 300 $\times$ 300 µm^2 (y, z) beam, the probed volume per image is 0.6 $\times$ 0.6 $\times$ 0.3 mm^3 (x, y, z).

Instead of piecing together data gathered from different experiments with an X-ray beam at different positions relative to the laser, the motion strategy (i.e., HDMD and base plate) used enabled us to obtain time-resolved data in a single experiment as the relative position of the X-ray beam to the laser was changing. The distance-to-time scale conversion is explained hereafter. For additional information, the deposition of one layer following the aforementioned motion strategy can be seen in Supplementary Animation 1.

A reference laser time scale (t_{ref}) is used instead of the distance scale to simplify data representation and interpretation (see Figure 1c). This scale is constructed based on the following considerations. In the reference frame of the sample, at any given instant, irrespective of the location probed by the X-rays, the laser is either approaching or moving away from that location at a constant speed of 10 mm.s^{-1} which is the printing speed. For the laser, the X-rays are probing a distance of $\pm$20 mm around the laser. Therefore, the reference time scale is $t_{\text{ref}} = d_{l-X}/v_{\text{substrate}} = 4$ s. To better understand this scale, consider a thought experiment where the substrate and HDMD are kept immobile with respect to the laboratory frame and the focusing head is moving at the printing speed of 10 mm.s^{-1}. The thought experiment and the present experiment will result in the same printing conditions for the sample and the same time t_{ref} to probe the locations within a distance of $\pm$20 mm with respect to the laser.

The acquired 2D diffraction patterns (Debye-Scherrer rings) were integrated azimuthally, with a code available at the beamline, into 36 cakes of 10° each taking into account the detector thickness to obtain 36 different I vs. 2θ line profiles. Single peak fitting was performed for each of the hkl peaks using a Pearson VII function combined with a linear function for the background to obtain the average position of each peak. In addition, azimuthal integration was also performed on the full Debye-Scherrer rings i.e., over the 360° angular range, for data representation in Figure 6b.

Lattice strains were calculated from the change in the average peak positions of each of the hkl peaks using:

$$\varepsilon^{hkl} = \frac{\sin\theta_0^{hkl}}{\sin\theta^{hkl}} - 1 = \frac{d^{hkl} - d_0^{hkl}}{d_0^{hkl}} \tag{1}$$

where ε^{hkl} is the lattice strain, θ_0^{hkl} is half of the strain-free diffraction angle, θ^{hkl} is half of the measured diffraction angle, d_0^{hkl} is the strain-free interplanar spacing, and d^{hkl} is the measured interplanar spacing of a given $\{hkl\}$ plane family. The strain-free lattice parameter was obtained from measurements of a matchstick-shaped sample extracted from the material printed with the same AM parameters. This geometry relieves macroscopic stresses in the extracted sample providing an ideal strain-free reference [36]. For the material investigated, the mean strain-free lattice parameter obtained from the four aforementioned reflections is $a_0 = 3.59730 \pm 0.00026$ Å.

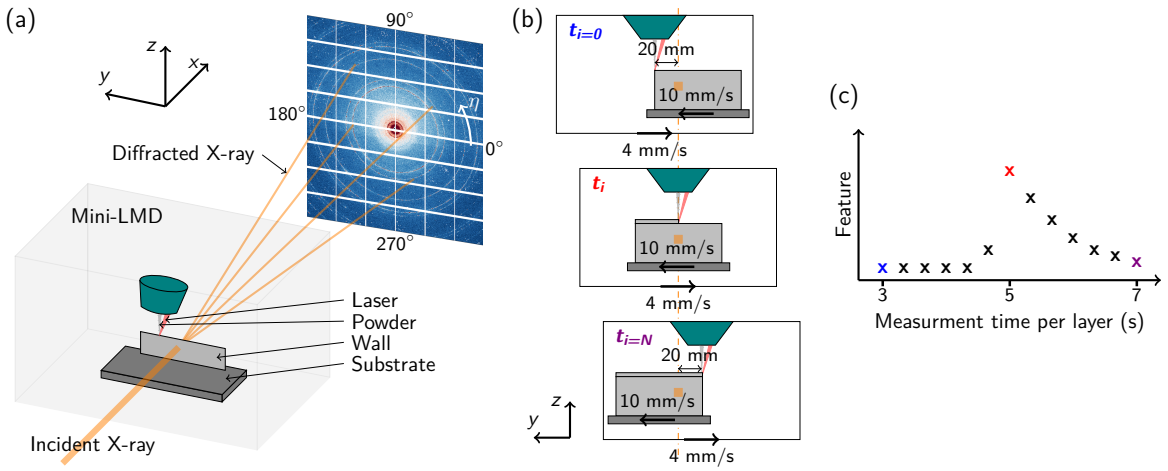

Figure 1: (a) experimental setup used during the *operando* synchrotron experiments, (b) printing strategy used during one layer addition from the point of view of the X-ray beam, (c) resulting data in the reference laser time scale. The orange square in (b) represents the X-ray beam position.

The arithmetic mean strain (ε^{lat}) of the 111, 200, 220, and 311 lattice plane families is used in this work. This choice was validated by comparing the average elastic strain against the elastic strain from the 311 lattice plane family as it best represents the bulk elastic properties for FCC materials [36] for the experimental residual strain maps presented in Figure 4. The difference between the two elastic strains, $\varepsilon^{\text{e}}_{311}$ and $\varepsilon^{\text{e}}_{\text{average}}$, is in the range of $\pm 0.025\%$. The latter estimate is used in this work to facilitate comparison with the simulated elastic strain.

The evolution of lattice strains along the horizontal ($\varepsilon^{\text{lat}}_{yy}$) and the vertical ($\varepsilon^{\text{lat}}_{zz}$) directions in the sample were evaluated from two $\pm 10°$ cakes with respect to the horizontal y (PD corresponding to 0° and 180° azimuthal angles) and the vertical z (BD corresponding to 90° and 270° azimuthal angles) directions (see Figure 1a for the convention).

The classic approach to decoupling elastic and thermal strains from XRD measurements involves analyzing the expansion and distortion of the entire Debye–Scherrer rings while utilizing temperature-dependent strain-free lattice parameters and assuming that the temperature evolution is known. However, this approach was not employed in this study due to significant drawbacks. For example, the strain-free lattice parameter can be determined during the process by averaging the diffraction peak over the Debye–Scherrer ring. This method, however, would completely neglect hydrostatic elastic strains, as these have the same effect as volume changes caused by temperature variations. Alternatively, the temperature-dependent strain-free lattice parameter can be estimated by extrapolating its room-temperature value to the actual temperature using the thermal expansion coefficient (through dilatometric tests). However, this approach may introduce non-negligible inaccuracies, as the computation of strains is highly sensitive to lattice parameters. More importantly, this classic decoupling approach requires precise temperature data, which is unavailable from this experiment alone, as no additional infrared measurements could be conducted using the mini-DED machine. Therefore, such a method was not applicable in this paper. This limitation highlights the need for alternative methods such as the experimental-modeling synergy proposed in this work.

2.3 Electron back-scattered diffraction (EBSD) investigation

EBSD measurements were carried out in an FEI quanta 650 FEG scanning electron microscope equipped with a Symmetry detector (Oxford Instruments) to investigate the microstructure, grain size, morphology, and orientation in the $y-z$ plane of the as-built sample (see Figure 1a). EBSD investigation was performed on a section of the sample extracted from the middle (along y) of the substrate and the as-built wall. This section was ground with abrasive paper up to 4000 grit, then using 1 µm diamond paste, followed by 50% diluted OPA solution, and finally etched using 10% oxalic acid for 10 s at 5 V. The EBSD acquisition was performed at 30 keV with a step size of 1.5 µm and an acquisition time of 0.6 ms. Each acquired image has a resolution of 750×500 µm^2. An overlap of 10% in each direction was used to reconstruct the full EBSD map. The maps were analyzed using the AZtec 6.0 SP1 software considering two phases: α ferrite (BCC) and γ austenite (FCC). Pixel confidence index before data post-processing was greater than 97.5%. Post-processing was done with the AZtec Crystal 3.0 software.

2.4 Model description, calibration, and validation procedure

The numerical simulation of the entire process relies on (i) a thermal analysis [5,34], and (ii) a finite element analysis (FEA) of the mechanics of the problem based on shell elements [7]. The thermomechanical model is weakly coupled in the sense that the effect of mechanics (i.e., elastic and plastic deformation) is neglected in the temperature calculation. This assumption is acceptable because both elastic and plastic distortions are sufficiently small such that mechanical dissipation plays a negligible role in changing temperature in comparison to the heat added by the laser. The simulation procedure is as follows: the temperature field history is first computed during the building of the entire part using a custom code developed in [5]. The computed thermal strains are then introduced as imposed strains in the mechanical model to compute the stresses and distortions. The detailed description and key assumptions of the model can be found in [5,7]. Below, only the governing equations, input parameters, and boundary conditions of the weakly coupled thermomechanical model are briefly recalled.

The thermal part of the model assumes that liquid metal is directly deposited at a temperature T_{dep} that is higher than the liquidus and computed as [37]:

$$T_{\text{dep}} = \frac{I\,\eta\,R_{\text{beam}}}{\sqrt{2\pi}\lambda_{\text{liq}}}\arctan\left(\frac{\sqrt{8\,D_{\text{liq}}t_{\text{beam}}}}{R_{\text{beam}}}\right) \tag{2}$$

where R_{beam} is the laser spot radius defined as two standard deviations of the Gaussian laser distribution, λ_{liq} and D_{liq} are respectively the thermal conductivity and diffusivity of the liquid metal, $I = 2\,P_{\text{beam}}/(\pi R_{\text{beam}}^2)$ is the laser intensity, η is the absorptivity of the powder, and $t_{\text{beam}} = \sqrt{2}\,R_{\text{beam}}/V_{\text{beam}}$ with V_{beam} being the laser beam velocity. Boundary conditions include thermal contact resistance between the top of the substrate and the bottom of the sample (due to the typical thickening of the sample at the bottom, and possible mismatch between sample and substrate grades), heat loss by convection on the other surfaces due to surrounding gas and by radiation, and the heat extracted by the cover/shielding gas. The cover gas effect has been modeled by directly imposing a volumetric heat loss that is extracted by the cover gas according to a Gaussian moving distribution [5]:

$$Q_{\text{gas}}(t) = 2\frac{H_{\text{gas}}}{h_x}(T - T_{\text{amb}})\exp\left(-2V_{\text{beam}}^2\frac{(t-t_n)^2}{R_{\text{gas}}^2}\right) \tag{3}$$

where T_{amb} is the ambient temperature, H_{gas} is the heat transfer coefficient (HTC) associated with the gas flow, R_{gas} characterizes the area affected by the gas flow, and h_x is the thickness of a bead (smallest portion of a modeled layer).

In addition, latent heat of fusion is taken into account during solidification. Some proportion η of the power is used to melt the powder, which is already taken into account in Equation (2), and some proportion η_{beam} may be absorbed by the layer on top of which the deposition is made. Assuming a Gaussian laser spot, the associated power per unit volume absorbed by the top layer is [5]:

$$Q_{\text{beam}}(t) = \frac{2\eta_{\text{beam}}P_{\text{beam}}}{\pi h_z R_{\text{beam}}^2}\exp\left(-2V_{\text{beam}}^2\frac{(t-t_n)^2}{R_{\text{beam}}^2}\right) \tag{4}$$

where h_z is the bead height, and t_n is the time of metal deposition for the considered 2D multilayer structure. It should be noted that the contribution of Equation (4) was not very high in [5,7,34] as the laser was coaxial with the nozzle spraying the powder. But in this study, the laser is tilted with respect to the spraying nozzle [35] so that a significant proportion of the laser is directly absorbed by the existing layer on top of which the metal deposition is made.

The mechanical part of the model [7] takes input from the thermal part. It is solved using the open source software Castem [38], and combines element birth and element activation techniques. The former progressively adds new elements to the existing mesh, while the latter involves using a single unchanging mesh of the part with very low stiffness and progressively assigning realistic stiffness and material properties to the elements. A hybrid strategy combining element birth and element activation is followed: each new layer is added to the existing mesh (with low stiffness) at the end of the dwell time, and then the real material properties are assigned to the first element (in the direction of laser motion) of this new layer when the laser begins printing this new layer. Meanwhile, at each time increment real stiffness is assigned to a single element in the wake of the laser. Since a thin-walled structure is considered, shell elements are used (i.e., 2D Reisner-Mindlin theory). The details of this implementation to compute the Cauchy stress field can be found in [7].

Temperature-dependent elasto-plastic behavior under infinitesimal strain assumption is considered with isotropic stiffness (which can be supported by the fact that crystallographic and morphological textures are not sufficient for the resulting stiffness anisotropy to play a major role), classical von Mises

plastic flow rule and kinematic hardening. Material properties are fitted from data at high temperatures obtained in [39] for the yield stress and in [40] for shear and Young's moduli, and at room temperature from data reported in previous studies [41, 42]. A linear temperature dependence is assumed for the Young's $E(T)$ and shear $\mu(T)$ moduli:

$$E(T) = E_0 \left(1 - \beta_E \left(T - T_0\right)\right) \tag{5}$$

$$\mu(T) = \mu_0 \left(1 - \beta_\mu \left(T - T_0\right)\right) \tag{6}$$

where $T_0 = 273.15$ K, E_0 is the Young's modulus at T_0, μ_0 is the shear modulus at T_0, and β_E and β_μ are fitting parameters. The thermal expansion coefficient α is assumed to be constant. The yield stress dependence on temperature is modeled using an exponential rule:

$$\sigma_Y(T) = \sigma_0 \left[1 + \beta_Y \, \exp\left(-\gamma_Y (T - T_0)\right)\right] \tag{7}$$

where σ_0 is the yield stress at high temperature, β_Y is a dimensionless coefficient, and γ_Y is a fitting coefficient. Note that the yield stress vs. temperature curve is provided in [7]. The kinematic hardening coefficient denoted by H_Y is assumed to be a constant. The values of the input parameters of the weakly coupled model are listed in Table 2.

All the material parameters except η and η_{beam} have been extracted from [5,7] for which a similar DED machine and the same material were used. The only difference between this study and the ones in [5,7] is the laser wavelength and the tilt angle with respect to the vertical direction, which requires calibrating η and η_{beam}. To do so, only the top layer is considered for calibration at very high temperatures when elastic strain is negligible and the lattice strain can be reasonably approximated to only have contributions from thermal strains. The computed temperature evolution is compared to the measured lattice strain and the absorptivity coefficients η and η_{beam} are calibrated to obtain a reasonable agreement. The mechanical computation is not calibrated as it only depends on temperature evolution and known temperature-dependent material parameters.

The validation procedure is twofold. First, the computed and measured residual elastic strain maps (i.e., over the entire structure after complete cooling) are compared. Second, the computed and measured transient lattice strain profiles (i.e., elastic+thermal strains) are compared for different layers. Since XRD techniques do not capture plastic strain, this contribution cannot be directly validated, but only indirectly as elastic strain strongly depends on the plastic flow.

2.5 New thermal and elastic strain estimates

Considering model assumptions and fitted model parameters (e.g., absorptivity), numerical predictions are not in perfect agreement with experimental data. To improve these predictions, one could use them as a reasonable starting point that should be corrected according to the experimental measurements to better estimate thermal and elastic contributions. Therefore, new elastic and thermal strain estimates are derived and respectively denoted by $\varepsilon_{yy}^{\text{est,e}}, \varepsilon_{zz}^{\text{est,e}}$ and $\varepsilon^{\text{est,th}}$ (where the superscript "est" stands for estimate). To that end, the distance between the strain estimates and the strains obtained from the numerical simulation (denoted by $\varepsilon_{yy}^{\text{num,e}}, \varepsilon_{zz}^{\text{num,e}}$ and $\varepsilon^{\text{num,th}}$ where the superscript "num" stands for numerical) is minimized under the strict constraint that the sum of elastic and thermal strain estimates exactly matches the measured lattice strains $\varepsilon_{yy}^{\text{lat}}$ and $\varepsilon_{zz}^{\text{lat}}$, which reads:

$$\begin{cases} (\varepsilon_{yy}^{\text{est,e}}, \varepsilon_{zz}^{\text{est,e}}, \varepsilon^{\text{est,th}}) = \underset{}{\text{argmin}} \quad J(\varepsilon_{yy}^{\text{est,e}}, \varepsilon_{zz}^{\text{est,e}}, \varepsilon^{\text{est,th}}) \\ \text{s.t.} \qquad \varepsilon_{yy}^{\text{est,e}} + \varepsilon^{\text{est,th}} = \varepsilon_{yy}^{\text{lat}} \quad \text{and} \quad \varepsilon_{zz}^{\text{est,e}} + \varepsilon^{\text{est,th}} = \varepsilon_{zz}^{\text{lat}} \end{cases} \tag{8}$$

where the cost function reads:

$$J(\varepsilon_{yy}^{\text{est,e}}, \varepsilon_{zz}^{\text{est,e}}, \varepsilon^{\text{est,th}}) = \int w_y \left(\varepsilon_{yy}^{\text{est,e}} - \varepsilon_{yy}^{\text{num,e}}\right)^2 + w_z \left(\varepsilon_{zz}^{\text{est,e}} - \varepsilon_{zz}^{\text{num,e}}\right)^2 + w_{\text{th}} \left(\varepsilon^{\text{est,th}} - \varepsilon^{\text{num,th}}\right)^2 \tag{9}$$

where the integral is considered over the duration of data recording for each given layer, and w_y, w_z and w_{th} are strictly positive weights. Note that the strict constraint in the minimization problem (8) implies that the measured lattice strains are considered as a "ground truth", while numerical results are corrected since the cost function (9) never converges to zero.

The solution of Equation (8) is obtained by direct differentiation of the corresponding Lagrangian and

Table 2: Input parameters.

Number of layers	N_{lay}	(-)	100
Substrate thickness	h_{sub}	(mm)	10
Initial substrate temperature	T^0_{sub}	(K)	300
Length of wall	L	(mm)	100
Layer height	h_z	(mm)	0.2
Layer thickness	h_x	(mm)	0.6
Laser beam radius	R_{beam}	(mm)	0.2
Laser beam speed	V_{beam}	(mm.s^{-1})	10
Laser beam power	P_{beam}	(W)	100
Dwell time	t_{dwell}	(s)	14
Powder absorptivity	η	(-)	0.4
Top layer absorption	η_{beam}	(-)	0.17
Liquidus temperature	T_{liq}	(K)	1726
Solidus temperature	T_{sol}	(K)	1607
Liquid thermal conductivity	λ_{liq}	(W.m^{-1}.K^{-1})	30
Liquid thermal diffusivity	D_{liq}	(m^2.s^{-1})	13×10^{-6}
Solid thermal conductivity	λ_{sol}	(W.m^{-1}.K^{-1})	21
Solid thermal diffusivity	D_{sol}	(m^2.s^{-1})	5.25×10^{-6}
Latent heat of fusion	L_f	(J.mm^{-3})	2.1
HTC part/air	H_{air}	(W.m^{-2}.K^{-1})	15
HTC part/build platform	H_{build}	(W.m^{-2}.K^{-1})	20000
HTC part/cover gas	H_{gas}	(W.m^{-2}.K^{-1})	300
Young modulus at 273.15 K	E_0	(MPa)	192835
Coefficient	β_E	(K^{-1})	4.2×10^{-4}
Shear modulus at 273.15 K	μ_0	(MPa)	77765
Coefficient	β_μ	(K^{-1})	4.3×10^{-4}
Thermal expansion coefficient	α	(K^{-1})	20×10^{-6}
High temperature yield stress	σ_0	(MPa)	66
Coefficient	β_Y	(-)	4.435
Coefficient	γ_Y	(K^{-1})	2.236×10^{-3}
Hardening coefficient	H_Y	(MPa)	1200

reads:

$$\begin{cases} \varepsilon^{\text{est,th}} = \dfrac{w_y\varepsilon^{\text{lat}}_{yy} + w_z\varepsilon^{\text{lat}}_{zz} - w_y\varepsilon^{\text{num,e}}_{yy} - w_z\varepsilon^{\text{num,e}}_{zz} + w_{\text{th}}\varepsilon^{\text{num,th}}}{w_y + w_z + w_{\text{th}}} \\ \varepsilon^{\text{est,e}}_{yy} = \varepsilon^{\text{lat}}_{yy} - \varepsilon^{\text{est,th}} \\ \varepsilon^{\text{est,e}}_{zz} = \varepsilon^{\text{lat}}_{zz} - \varepsilon^{\text{est,th}} \end{cases} \tag{10}$$

The strain fields provided in Equation (10) should be interpreted as estimates of elastic and thermal strains correcting the initial numerical predictions of elastic and thermal strains. Note that, if the model predictions were in perfect agreement with the experiment, then the strain estimates would match exactly with the numerical predictions of the elastic and thermal strains. Reciprocally, the greater the discrepancy between numerical simulations and measurements, the greater the correction for numerical predictions of elastic and thermal strains. Thus, the correction is more significant around 5 s where the agreement between the numerical model with the experiment is not as good as for the rest of the strain profiles (see Figure 8).

As is the case for all minimization techniques, estimates (10) depend on the chosen weights (i.e., w_y, w_z, w_{th}). This necessary choice allows us to specify how the correction of numerical results is performed. Since the thermal contribution is an order of magnitude greater than the elastic contributions, the weights are chosen to normalize each contribution, that is to say $w_y = 1/\left\|\varepsilon^{\text{num,e}}_{yy}\right\|$, $w_z = 1/\left\|\varepsilon^{\text{num,e}}_{zz}\right\|$ and $w_{\text{th}} = 1/\left\|\varepsilon^{\text{num,th}}\right\|$, where $\|.\|$ denotes the classical L^2-norm considered over the duration of data recording. This choice is well justified by the fact that elastic strains have the same level of confidence than thermal strain and should therefore be corrected in similar proportion. Without normalization, the correction would almost exclusively affect elastic strains because they are much smaller than thermal strains and would therefore not significantly penalize the cost function (9). As a result, the new thermal strain estimate $\varepsilon^{\text{est,th}}$ would be almost identical to the initial numerical thermal strain $\varepsilon^{\text{num,th}}$, while

elastic estimates $\varepsilon_{yy}^{\text{est,e}}$ and $\varepsilon_{zz}^{\text{est,e}}$ would be nearly freely and independently adjusted so that the constraint is respected. This situation would correspond to a quasi-perfect confidence in the numerical thermal analysis, and almost no confidence in the subsequent mechanical computation. Since thermal and mechanical simulations have each been validated both in the present and previous studies [7, 43], there is no reason to favor one over the other. As a result, thermal and elastic strain contributions should be normalized in the cost function (9) to evenly distribute the confidence between the two models.

The relationships in (10) imply that measurement noise is introduced without amplification in the thermal and elastic strain estimates. Note that noise filtering techniques have not been used because noise amplitude was reasonable and we wanted to avoid smoothing the signal when the laser is in the vicinity of the observed zone.

Finally, note that the estimates in (10) can be improved if the full diffraction ring is considered. However, this analysis is more involved and since in this work we are mainly concerned with obtaining the temperature and in-plane normal stress estimates, which are encoded inside $\varepsilon_{yy}^{\text{lat}}$ and $\varepsilon_{zz}^{\text{lat}}$ components, the cost function in (9) is deemed to be sufficient for this purpose.

The overall experimentally corrected numerical approach is summarized in Figure 2.

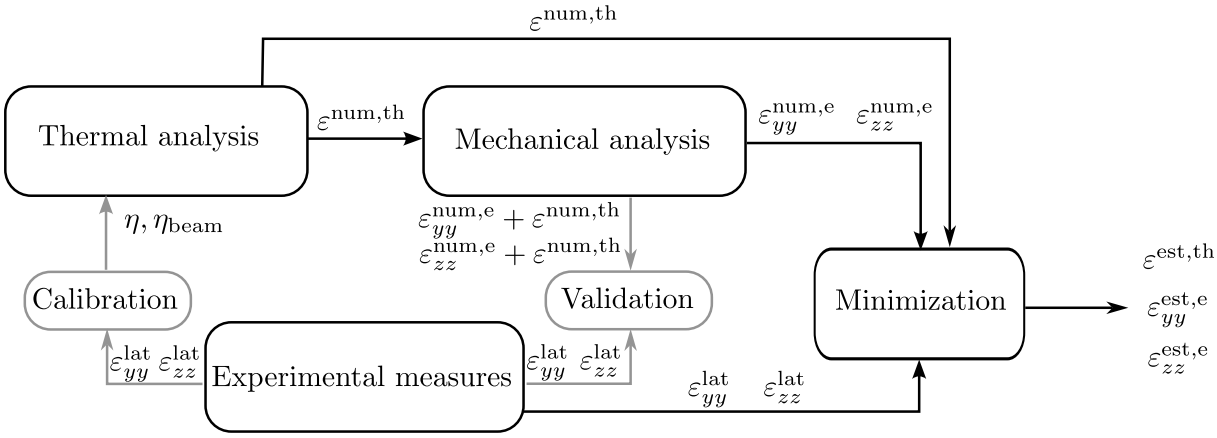

Figure 2: Chart summarizing the experimentally corrected numerical scheme to estimate elastic and thermal strains.

3 Results

3.1 Microstructure characterizations

EBSD imaging (Figure 3a) was performed on the as-built microstructure in the $y-z$ plane to obtain information about texture, grain size, and morphology. A 10° misorientation threshold was used to highlight grain boundaries. Along the wall height (z) a fine and homogeneous microstructure is observed with grains having a preferred inclination towards PD. At the bottom of the wall close to the substrate, the grains are more elongated than the ones in the middle and the top, however, their sizes are similar along BD. The grain size in the entire wall was quantified via their observed surface area and a monomodal distribution was obtained. The first quartile, the median, and the third quartile of the grain surface area distribution are respectively 101 µm^2, 268 µm^2, and 700 µm^2 (the corresponding equivalent diameters are 11.3 µm, 18.5 µm, and 29.9 µm). The {100} pole figure shows a preferred ⟨001⟩ orientation of the grains along the y direction of the wall (Figure 3b). Nevertheless, the observed texture can be considered weak. The two other pole figures show a negligible preferred orientation. The observed weak texture and the similarity in grain size across the sample supports the use of large-scale simulations with isotropic material properties at the part scale.

3.2 Residual elastic strains - measurements and predictions

Following the justification of using isotropic material properties in Section 2.4, simulations of the building of 100-layer walls are performed and the predicted residual elastic strains are compared with those obtained from synchrotron XRD measurements. Figure 4a and c show the measured mean residual elastic strain distribution (a) $\varepsilon_{yy}^{\text{e}}$ and (c) $\varepsilon_{zz}^{\text{e}}$ within the wall at room temperature at the end of the building. Residual strains are non-uniform across the sample, both along the BD and PD, due to the thermomechanical conditions arising during building from the sample geometry, boundary conditions, and heat-matter interactions. Close to the center of the sample, residual strains are tensile along PD

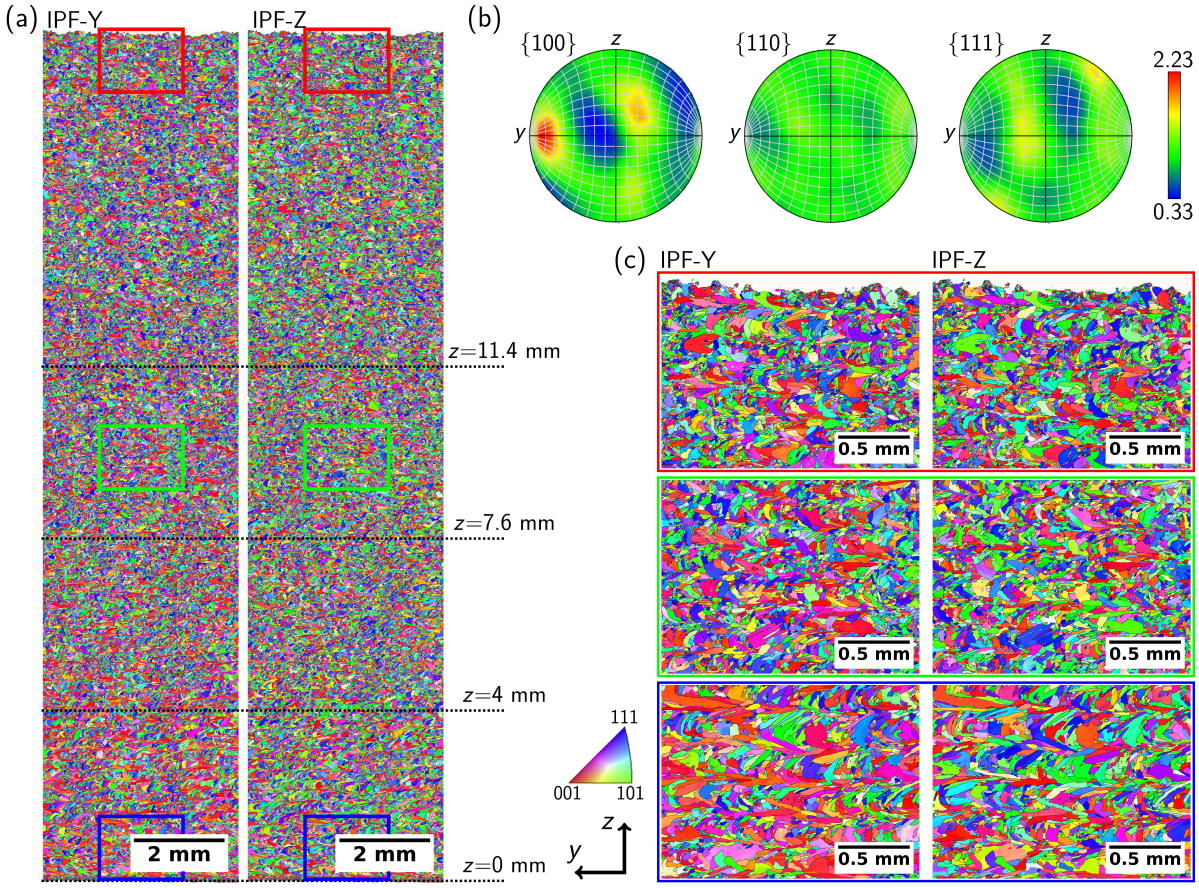

Figure 3: (a) Inverse pole figure y (IPF-Y) and z (IPF-Z) orientation maps along the $y-z$ plane obtained via EBSD, (b) the corresponding pole figures, and (c) zoomed IPF-Y and IPF-X maps from the bottom (blue zone), middle (green zone), and top (red zone) of the wall in (a). The z position of the three regions investigated via *operando* synchrotron XRD are shown in (a). The coordinate axes and IPF color legend are common to (a) and (c).

and compressive along BD. Along PD, the highest magnitude occurs in the last few deposited layers; according to a recent study [35], the magnitude is the highest in the ∼5th layer below the topmost layer. However, at the edges of the wall ($y = -50$ to -40 mm and $y = 40$ to 50 mm) the opposite trends, compression along PD and tension along BD, are observed.

The simulation predicted residual elastic strains are shown in Figure 4b and d. In general, they are in good agreement with the experimentally measured ones. Note that the scale has been chosen to emphasize discrepancies between measured and simulated strains as only a few pixels are out of the range $[-0.2\%, 0.2\%]$ and reach a maximum of ∼0.4%. At the edges of the sample, some discrepancies are visible between the measured and simulated strains because, unlike the simulated geometry, the printed thin-walls are not perfectly rectangular. In addition, a residual stress profile along PD at $z = 10$ mm is presented in Figure 5 to better emphasize local discrepancy between experimental and numerical results. Despite this difference, the Pearson product-moment correlation coefficient between experimental and simulated results is 0.9 for the PD and 0.86 for the BD strains, which consolidates the excellent match and validates a significant part of the model and its assumptions [5, 7]. Notably, simulations capture the asymmetry in the elastic strains with respect to $y = 0$ (not evident in the experimental measures because of edge effects) due to the unidirectional printing strategy from $y = -50$ mm to $y = 50$ mm.

Based on this match, this model is used to study the effect of elastic strain (ε^e) on the temperature (T) estimated from the measured lattice strain (ε^{lat}). While a good match of the residual lattice strains does not automatically imply a good match of the transient lattice strains, it nevertheless provides a higher degree of confidence in the simulation predictions. Nevertheless, as shall be seen in Section 3.3), the model predictions are also validated against *operando* measurements.

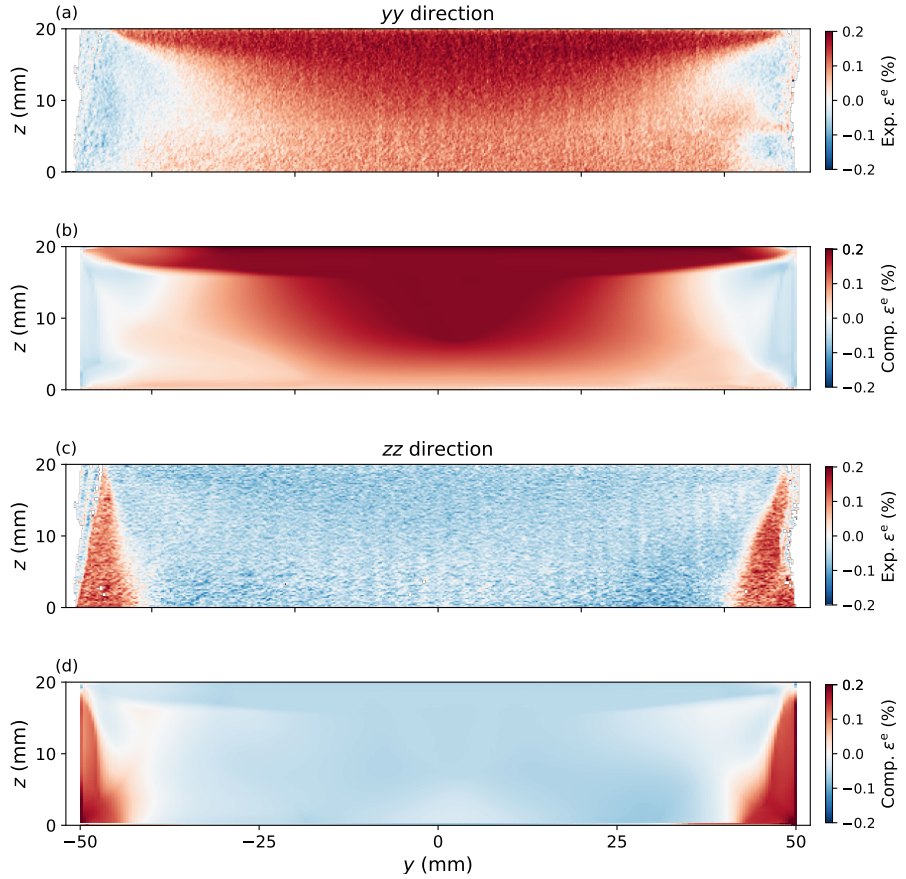

Figure 4: (a, c) Experimental (Exp.) and (b, d) computed (Comp.) residual strain maps at room temperature after the building of 100 layers: (a and c) ε^{e}_{yy} (PD) and (b and d) ε^{e}_{zz} (BD). Experimental measurements were done with a scanning step of 200 µm in both directions, while the mesh is composed of 400 µm × 200 µm elements. The center of the wall was set at $y = 0$ mm and the top of the substrate at $z = 0$ mm. Printing started at y = -50 mm and ended at $y = 50$ mm. The scale bar is set in the range [-0.2%, 0.2%] to facilitate visualization because only a very small amount of points, which are difficult to visualize, show values beyond this range.

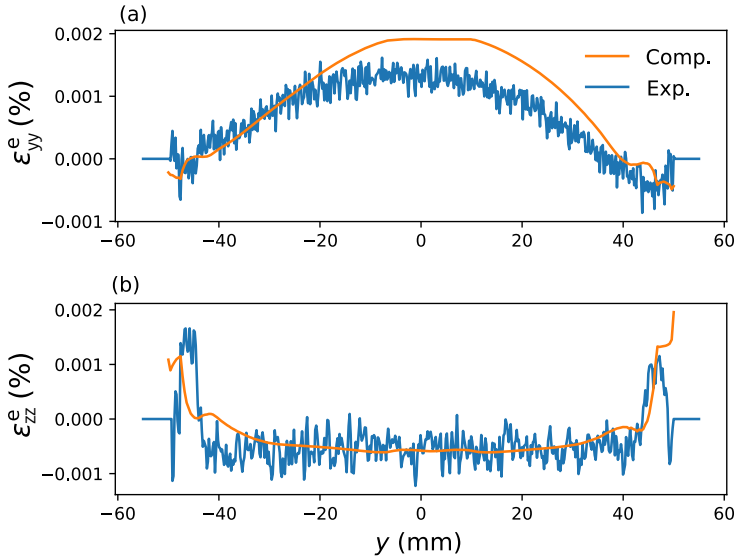

Figure 5: Experimental and computed residual strain profiles along the PD at $z = 10$ mm at room temperature after building of 100 layers (a) ε^{e}_{yy} (PD) and (b) ε^{e}_{zz} (BD).

3.3 *Operando* synchrotron XRD measurements and validation of simulations

Figure 6 shows some of the diffraction patterns obtained during the addition of the 20$^{\text{th}}$ layer, i.e., L_{20} ($z = 4$ mm in Figure 3a); the time $t = 0$ s in Figure 6 and the text below refers to the beginning of the printing of a layer. Focusing first on the 2D diffraction patterns in Figure 6a, at $t = 5.06$ s, an amorphous pattern is observed due to the presence of the liquid phase along with some Debye-Scherrer rings arising from the powder and the previously deposited layer. Then, at $t = 5.12$ s, the material has solidified and Debye-Scherrer rings with distinct large spots are observed due to the presence of coarse austenite grains. In addition, Debye Scherrer rings are also observed due to the colder powder illuminated by the X-ray beam as the focusing head passes overhead (the powder lies within the same $y - z$ plane as the manufactured wall). Finally, at $t = 5.32$ s, only the Debye-Scherrer rings from the solidified material are visible.

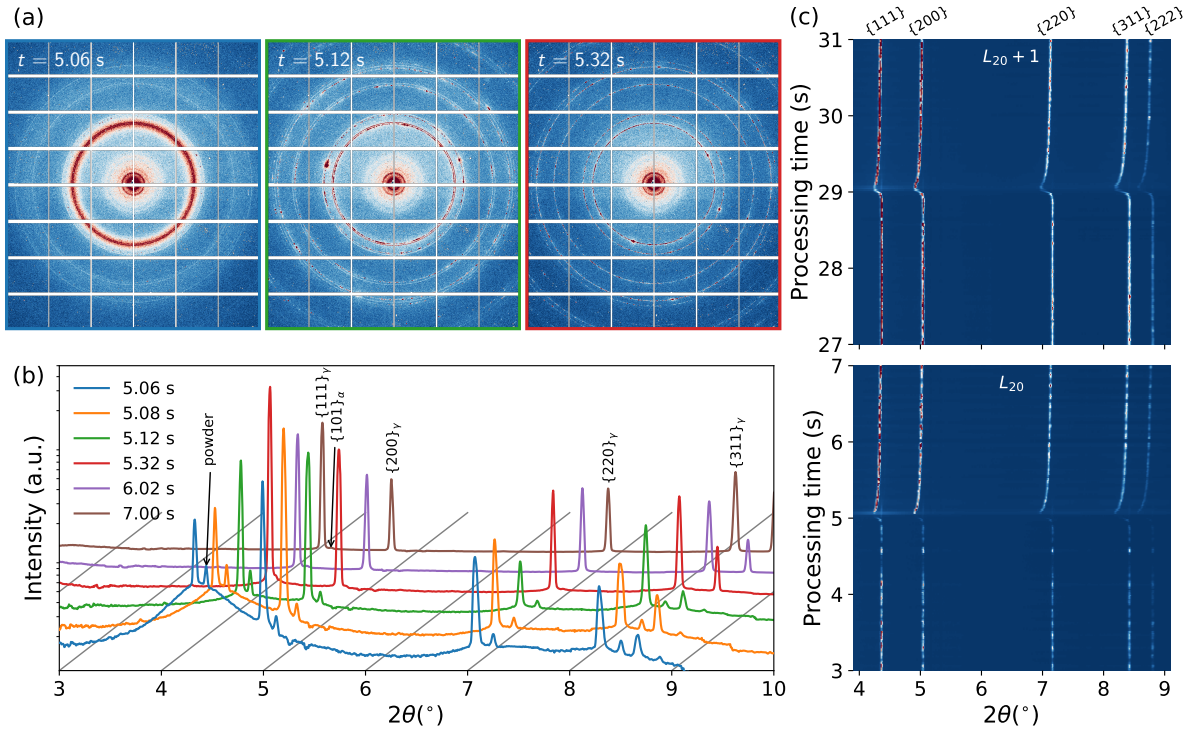

Figure 6: (a) 2D detector images at different processing times during AM of layer L_{20}, (b) evolution of diffraction profiles of layer L_{20} while deposited at different processing times, and (c) stacked diffraction profiles over processing time during the addition of 2 layers, L_{20} and $L_{20} + 1$. The colors used to enclose the detector images in (a) correspond to the colors of the diffraction profiles shown in (b).

To better understand the appearance and disappearance of different phases, the Debye-Scherrer rings are integrated over the azimuthal angle η to obtain diffraction line profiles I vs. 2θ as a function of time. At $t = 5.06$ s, the diffraction peaks from the powder and the previously deposited layer are visible; recall that the X-ray beam height is slightly larger than the layer height and it interacts with the layer below. The amorphous pattern, barely visible at $t = 5.12$ s, shows the end of solidification following which the solid phase is mainly austenitic. Just after solidification and until the end of printing of the layer, a faint {101} diffraction peak corresponding to the ferrite phase is obtained, although it is not visible in Figure 6b. Rietveld refinement estimates the ferrite phase fraction to be lower than 0.5 wt% at room temperature. Figure 6c shows the processing time vs. 2θ plot for the different profiles for layers L_{20} and $L_{20} + 1$. As the laser approaches the investigated region, all the diffraction peaks shift towards the lower 2θ angles because of the temperature increase. The opposite trend is observed after melting and during solidification i.e., all the diffraction peaks shift towards higher 2θ angles because of the temperature decrease.

Figure 7 shows the mean lattice strain $\varepsilon_{yy}^{\text{lat}}$ and $\varepsilon_{zz}^{\text{lat}}$ evolution due to the intrinsic heat treatment generated during AM as a function of the measurement time per layer for building starting at layer height $z = 4$ mm i.e., with the deposition of layer L_{20}.

Focusing first on $\varepsilon_{yy}^{\text{lat}}$ (Figure 7a), during the printing of L_{20}, the signal from $t = 3$ s to 5 s is coming from the previously printed layer L_{19}. Starting with a slight tensile residual strain, the lattice parameter gradually decreases until $t = 5$ s. When the molten material is deposited at $t = 5$ s, it becomes impossible to fit the data because of the absence of diffraction peaks (amorphous patterns coming from the liquid).

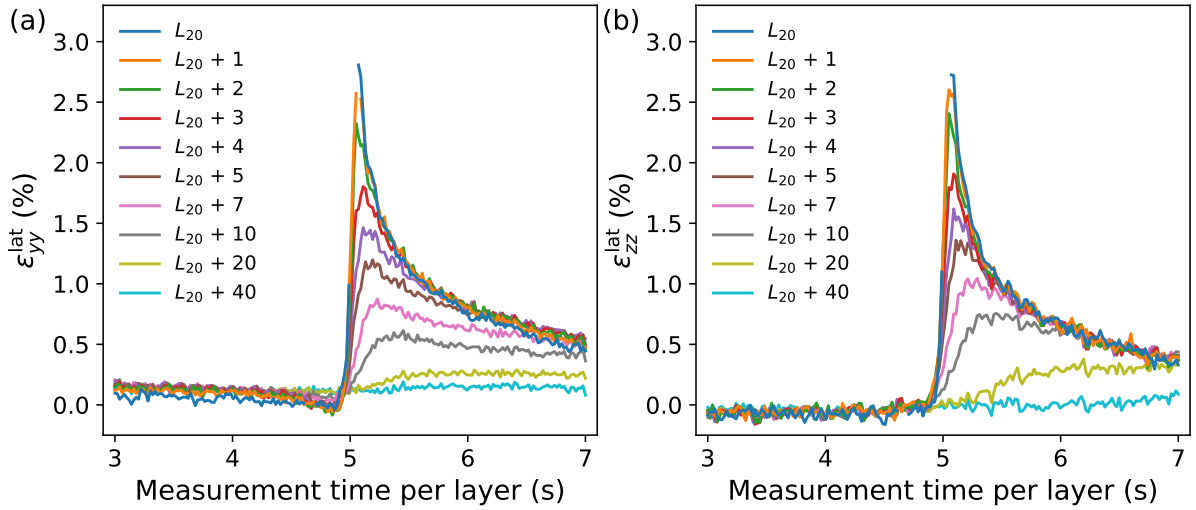

Figure 7: Evolution of measured lattice strains (a) ε_{yy}^{lat} (along PD) and (b) ε_{zz}^{lat} (along BD) at $z = 4$ mm above the substrate during the LMD process (see Figure 3 for reference to heights).

Discernible diffraction patterns reappear only after solidification ($t > 5$ s), at which point ε_{yy}^{lat} is very high due to thermal expansion and it continuously decreases due to subsequent thermal contraction. After cooling down to room temperature (at $t = 3$ s for layer $L_{20} + 1$), the probed volume on layer L_{20} has a residual ε_{yy}^{lat} of ~0.18%; this result is consistent with our previous study focusing on the {400} family of single grains in the bulk [35]. This tensile strain can be explained by the temperature gradient mechanism [44] occurring during local cooling of a single-phase material and more recently demonstrated in the specific case of a moving laser interacting with the same DED 316L stainless steel [45] as used in this work. Next, during the printing of $L_{20} + 1$, as the laser approaches the probed volume, the residual ε_{yy}^{lat} shows a continuous decrease until ~4.8 s due to a decrease in interplanar spacing. The contraction is gradual from 3 s to ~3.8 s, but it steepens after ~3.8 s as the laser comes closer to the probed volume. This contraction is the result of the restricted expansion of the heated material by the surrounding cooler material leading to the development of compressive strains [44, 46]; similar contractions have been reported during laser processing of a Ti6Al4V alloy [21], laser-based powder bed fusion AM of Inconel 625 alloy [46], L-DED AM of high carbon steel [17] via *operando* synchrotron experiments, as well as predicted with a numerical thermomechanical model for 316L [45] and Inconel 718 alloy [47]. After ~4.8 s, ε_{yy}^{lat} increases due to the heat input caused by the proximity of the laser with the probed volume and then decreases after the passage of the laser ($t > 5$ s), similar to the deposition of L_{20}.

Meanwhile, contrary to ε_{yy}^{lat}, ε_{zz}^{lat} starts with a compressive residual strain at the start of the deposition of L_{20} (Figure 7b). It slightly increases until the laser approaches very close to the probed region. Then, similar to ε_{yy}^{lat}, ε_{zz}^{lat} increases and the fit is lost due to the presence of a local melt pool. After solidification, it reappears and ε_{zz}^{lat} exhibits a similar decrease as ε_{yy}^{lat}. A compressive strain is obtained after cooling down to room temperature (see $L_{20} + 1$ at 3 s). The deposition of the next layer $L_{20} + 1$ results in the same trend as the deposition of layer L_{20} but with lower amplitudes. The increase in ε_{zz}^{lat} during the laser approach corresponds to the decrease in ε_{yy}^{lat} due to the Poisson effect.

After three added layers ($L_{20} + 3$) and until the end of AM processing, the maximum lattice strain reached along BD is higher than along PD. The aforementioned lattice strain evolution cycles along the two directions repeat until the end of the AM process but the magnitude of the contraction and expansion decrease with the number of added layers.

Evolution of ε_{yy}^{lat} and ε_{zz}^{lat} as a function of added layers and measurement time was also studied at heights $z = 7.4$ mm and 11 mm above the substrate (see Supplementary Figure A1). Both ε_{yy}^{lat} and ε_{zz}^{lat} evolutions at these heights were similar to the ones shown in Figure 7. However, the further the investigated position (i.e., higher z) from the substrate, the higher the maximum strain reached during each cycle and the lower the cooling rate. This is because the substrate acts as a heat sink and the regions closer to the substrate conduct away the heat faster than the regions away from the substrate.

Figure 8 shows the comparison between the experimental and simulated ε_{yy}^{lat} and ε_{zz}^{lat} lattice strain (thermal + elastic) profiles for the addition of five layers starting from the 20th layer (i.e., $z = 4$ mm); only five layer additions are shown for a clear interpretation. A similar comparison is shown for the 37th and 55th layers (i.e., $z = 7.4$ mm and $z = 11$ mm, respectively) in Supplementary Figure B2. A good quantitative agreement with the experimental results is obtained, even though the computed lattice

strain kinetics show steeper slopes around 5 s than in the experiment. These steeper slopes are due to the fact that heat fluxes along the PD have been neglected i.e., the temperature computed in the observation zone is not affected by the laser before it enters the observation zone. Combining all these results, it can be concluded that the simulations correctly capture the residual strains and the lattice strain evolution.

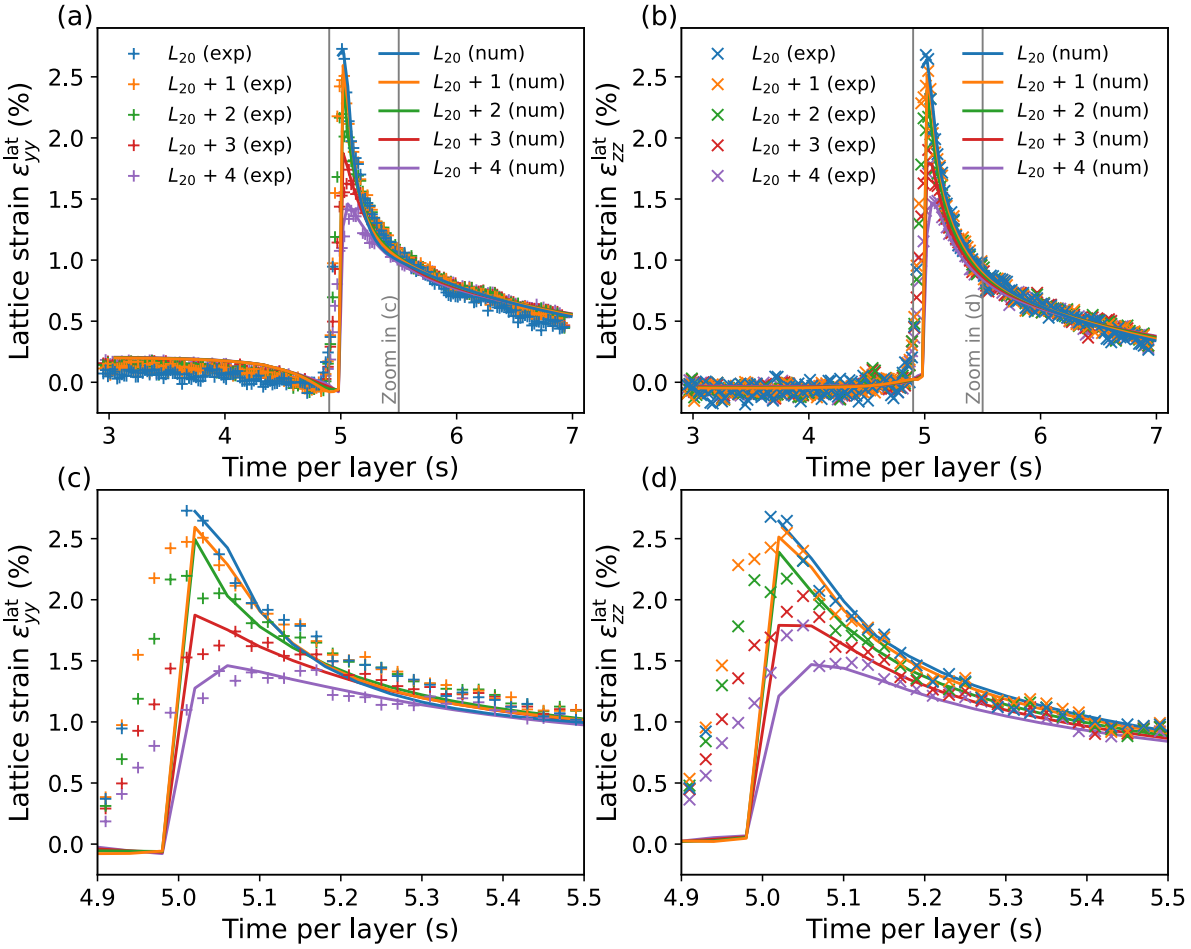

Figure 8: Computed and measured strain evolution of (a) $\varepsilon_{yy}^{\text{lat}}$ (along PD) and (b) $\varepsilon_{zz}^{\text{lat}}$ (along BD) at z = 4 mm above the substrate during the LMD process (see Figure 3 for reference to heights). Zooms of the computed and measured strain evolution during the cooling of (a) and (b) are shown respectively in (c) and (d).

3.4 Thermal and elastic strain estimates

The direct comparison between *operando* synchrotron XRD experiments and large-scale numerical simulation of AM process showed that the proposed numerical model not only correctly captures the final residual strain but also the temperature and elastic strains during the fabrication process. Therefore numerical results can be used as a reasonable initial guess to compute the experimentally corrected thermal and elastic strain estimates using (10). Figure 9 shows these strain estimates during the addition of five layers starting from 20th layer (i.e., z = 4 mm). Non-negligible elastic strain variations take place when the temperature reaches its maximum (i.e., around 5 s). In this region though, the elastic strains are usually neglected as the lattice strain (i.e., elastic+thermal strain) is usually interpreted as only composed of the thermal strain to estimate temperatures. As shown in Figure 9, such an assumption is indeed legitimate as the thermal strain is one order of magnitude larger than elastic strains near the temperature peak (i.e., around 5 s). However, correcting numerical results as done in Equation (10) not only improves the estimation of temperature profiles but also enables us to estimate how stresses evolve during fabrication.

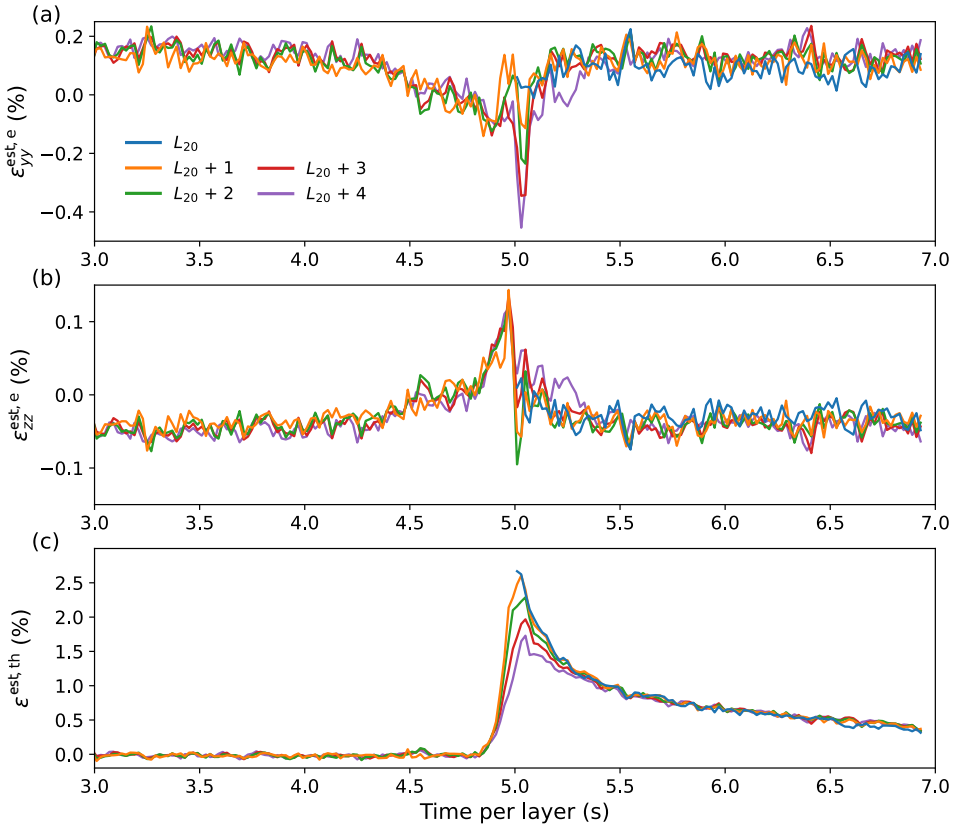

Figure 9: Strain estimates from Equation (10) at $z = 4$ mm: (a) $\varepsilon_{yy}^{\mathrm{est,e}}$, (b) $\varepsilon_{zz}^{\mathrm{est,e}}$ and (c) $\varepsilon^{\mathrm{est,th}}$.

4 Discussion

The classical temperature estimate obtained by attributing all the lattice strains to thermal strains can be computed as:

$$T_{ii}(t) = \frac{\varepsilon_{ii}^{\mathrm{lat}}(t)}{\alpha} + T_{\mathrm{ref}}, \qquad i = y, z \tag{11}$$

Note here that the subscripts yy and zz refer to the portions along y and z of the caked 2D Debye Scherrer patterns from which the lattice strains have been extracted to obtain the classical temperature estimate; they should not be confused as being components of a second-order tensor because temperature is a scalar and by definition it cannot have different components.

Meanwhile, the proposed temperature estimate reads:

$$T(t) = \frac{\varepsilon^{\mathrm{est,th}}(t)}{\alpha} + T_{\mathrm{ref}} \tag{12}$$

where $\varepsilon^{\mathrm{est,th}}(t)$ is the thermal strain estimate given in Equation (10) (conventionally defined by considering the room temperature T_{ref} as a reference since the lattice strain was computed using the strain-free room temperature lattice parameter a_0 as a reference).

To analyze in detail the effect of the new estimate of thermal strain on the estimation of temperature profiles, the following relative gap is introduced:

$$\delta_{ii}(t) = 100 \left(\frac{T_{ii}(t) - T(t)}{T(t)} \right), \qquad i = y, z \tag{13}$$

The temperature estimates T, T_{yy}, T_{zz} are presented in Figure 10a and c and the relative gaps δ_{yy}, δ_{zz} are presented in Figure 10b and d. For better readability, these figures are presented only for the 20^{th} layer with either 0 or 4 layers added above this layer; similar results are obtained for subsequent temperature cycles and other layers added and hence they are not shown. Relative gaps increase in absolute value during cooling as elastic contributions become more significant (see Figure 10). It should also be noted that relative gaps according to the BD are roughly three times as small in absolute value as those obtained for the PD with respectively 4% and 13% on average over the profiles presented in Figure 10b and 6% and

18% on average over the profiles presented in Figure 10d, which allows estimating temperature directly from the lattice strain along the BD with relatively good accuracy. But note that this only pertains to the studied simple case, which is DED of a single-pass-per-layer thin-wall geometry using a single-phase material (negligible solid-state phase transformations). The results will differ for metals and alloys undergoing solid phase transformation and more complex geometries.

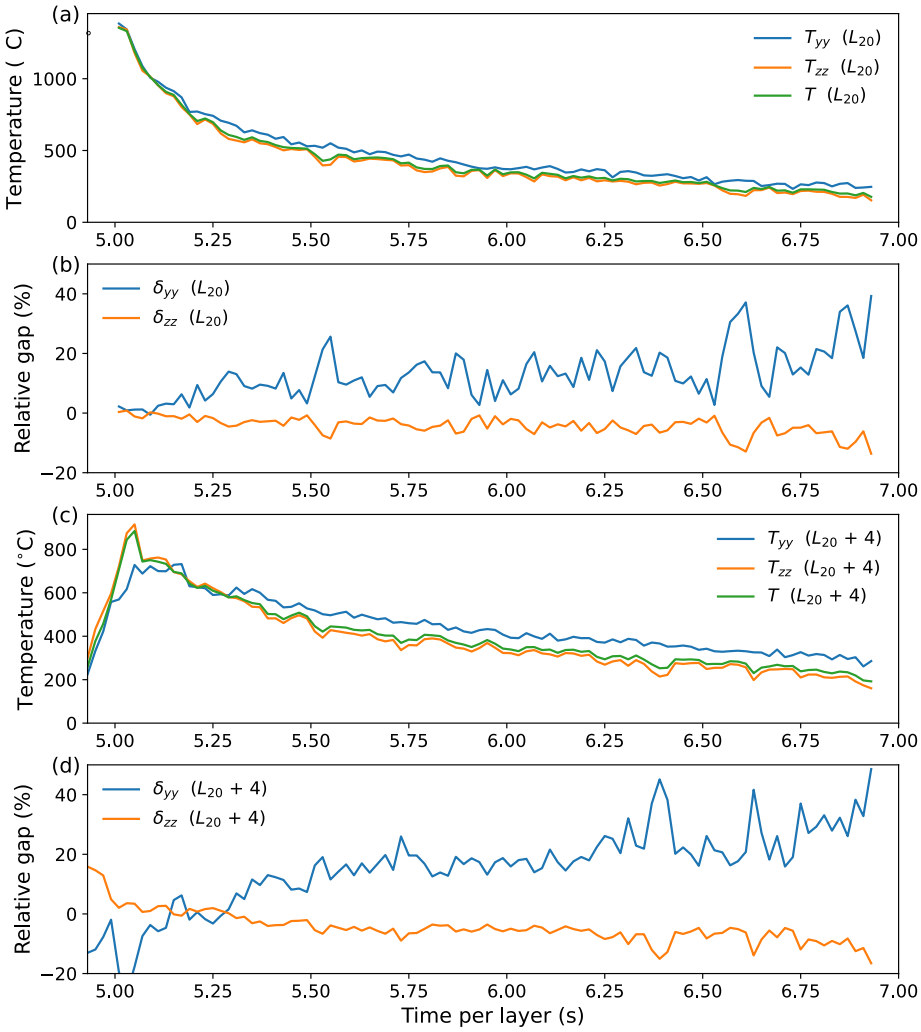

Figure 10: Profiles of experimental temperature estimates T_{yy}, T_{zz}, T respectively derived from the lattice strains $\varepsilon^{\text{lat}}_{yy}, \varepsilon^{\text{lat}}_{zz}$ or the estimate of the thermal strain using the decoupling procedure $\varepsilon^{\text{est,th}}$ (a) for the 20th layer currently deposited (i.e., without additional layer) (c) for the 20th layer with 4 additional deposited layers. Relative gaps δ_{yy}, δ_{zz} between T_{yy} and T and between T_{zz} and T (b) for the 20th layer currently deposited (i.e., without additional layer) (d) for the 20th layer with 4 additional deposited layers.

Secondary surface temperature measurements using bi-chromatic infrared technology (i.e., camera or pyrometer) would theoretically enable to validate that the proposed temperature estimate T is indeed an improvement in comparison to the classical temperature estimates T_{ii} (with $i = y, z$). However, such infrared measurements were impossible to perform due to the very limited room available in the mini-DED machine.

As already mentioned the proposed strategy of correcting numerical predictions to be perfectly consistent with experimental data not only improves the temperature estimate but also provides reliable elastic strain estimates that allow computing the transient stresses occurring during the process. For instance using the temperature-dependent elastic properties listed in Table 2 and the temperature estimate T, one can compute the estimates of stress profiles σ_{yy}, σ_{zz}, under the plane stress assumption, as shown in Figure 11. Non-negligible stress variations are observed in the very region where elastic strains are usually neglected.

Considering existing attempts [16, 17] to improve temperature estimates by simply integrating the experimental data over the full ring, i.e., $\eta \in [0°, 360°]$, we next test whether one could avoid using thermomechanical simulations of the process to estimate thermal and elastic strains by only relying on

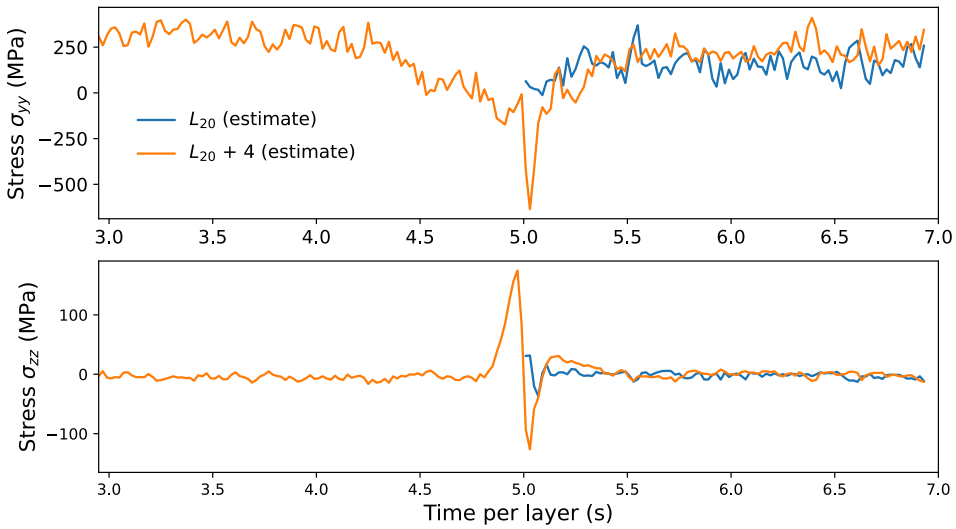

Figure 11: Stress estimates at the center of the 20th layer during the deposition of this layer and during the addition of the 4th layer above it.

simple integration rules for the Debye-Scherrer rings. If there exists a tractable azimuthal angle η for which at least one diagonal component of the elastic strain is negligible, then one could decouple thermal and elastic strain contributions; this approach has been used recently to estimate temperature evolution during neutron diffraction experiments [48]. To that end, η may be adjusted to change the coordinate system (y, z) by a rotation to obtain a secondary coordinate system denoted by y', z' so that the elastic strain components in this new system read:

$$\begin{cases} \varepsilon^{\mathrm{e}}_{y'y'} = \varepsilon^{\mathrm{e}}_{yy} \cos^2(\eta) + \varepsilon^{\mathrm{e}}_{zz} \sin^2(\eta) + 2\,\varepsilon^{\mathrm{e}}_{yz} \cos(\eta)\,\sin(\eta) \\ \varepsilon^{\mathrm{e}}_{z'z'} = \varepsilon^{\mathrm{e}}_{yy} \sin^2(\eta) + \varepsilon^{\mathrm{e}}_{zz} \cos^2(\eta) - 2\,\varepsilon^{\mathrm{e}}_{yz} \cos(\eta)\,\sin(\eta) \end{cases} \tag{14}$$

where the considered strains are extracted from the numerical simulation as shear strain is not directly estimated from XRD measurements. Thus, the angle η at which $\varepsilon^{\mathrm{e}}_{y'y'} = 0$ or $\varepsilon^{\mathrm{e}}_{z'z'} = 0$ is obtained as:

$$\begin{cases} \eta = \arctan\left(-\dfrac{\varepsilon^{\mathrm{e}}_{yz}}{\varepsilon^{\mathrm{e}}_{zz}} \pm \sqrt{\left(\dfrac{\varepsilon^{\mathrm{e}}_{yz}}{\varepsilon^{\mathrm{e}}_{zz}}\right)^2 - \dfrac{\varepsilon^{\mathrm{e}}_{yy}}{\varepsilon^{\mathrm{e}}_{zz}}}\right) \\ \text{if } \left(\varepsilon^{\mathrm{e}}_{yz}\right)^2 \geq \varepsilon^{\mathrm{e}}_{yy} \text{ and } \varepsilon^{\mathrm{e}}_{zz} \neq 0 \end{cases} \quad \text{or} \quad \begin{cases} \eta = \arctan\left(\dfrac{\varepsilon^{\mathrm{e}}_{yz}}{\varepsilon^{\mathrm{e}}_{yy}} \pm \sqrt{\left(\dfrac{\varepsilon^{\mathrm{e}}_{yz}}{\varepsilon^{\mathrm{e}}_{yy}}\right)^2 - \dfrac{\varepsilon^{\mathrm{e}}_{zz}}{\varepsilon^{\mathrm{e}}_{yy}}}\right) \\ \text{if } \left(\varepsilon^{\mathrm{e}}_{yz}\right)^2 \geq \varepsilon^{\mathrm{e}}_{zz} \text{ and } \varepsilon^{\mathrm{e}}_{yy} \neq 0 \end{cases} \tag{15}$$

If both $\left(\varepsilon^{\mathrm{e}}_{yz}\right)^2 < \varepsilon^{\mathrm{e}}_{yy}$ and $\left(\varepsilon^{\mathrm{e}}_{yz}\right)^2 < \varepsilon^{\mathrm{e}}_{zz}$, then one can only minimize $\left(\varepsilon^{\mathrm{e}}_{y'y'}\right)^2$ or $(\varepsilon^{\mathrm{e}}_{z'z'})^2$. The maximum orientation given by Equation (15) is presented in degrees in Figure 12. Large erratic variations take place when the laser is near the observation zone (i.e., between 4.5 and 5.5 s) due to the development of shear strains (see Figure B3 in the Supplementary material). However, in the current simple case, for $T < 500$ °C (i.e., $t > 5.7$ s) a good estimate of the temperature can be obtained by using a given η angle. Therefore, a rule of thumb would be very difficult to establish and any such rule would be inaccurate over the full temperature range.

5 Conclusion

Operando synchrotron X-ray diffraction (XRD) experiments were performed during AM – via the laser-based direct energy (L-DED) deposition process – of a 316L stainless steel and used to obtain the lattice strain evolution as a function of time. In addition, the residual elastic strain distribution in the entire sample was measured. These experimental results were used to validate a large-scale and fast numerical thermomechanical model. Good agreements were found between the experimentally measured and simulation predicted transient lattice strains and the final residual elastic strain distributions.

Then, elastic and thermal strain predictions computed with the numerical simulation are corrected to be perfectly consistent with experimental data. To do so, the distance between strain estimates and strains computed with the fast numerical simulation has been minimized under the constraint that the sum of thermal and elastic strain estimates exactly matches the measured lattice strain. This strategy not only slightly improved the estimation of temperatures compared to classical data interpretation neglecting

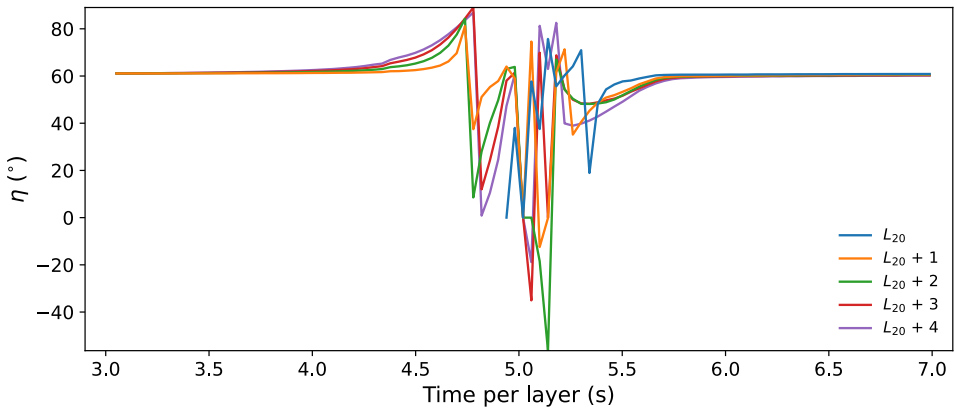

Figure 12: Maximum azimuthal angle η for which at least one diagonal component of the elastic strain tensor vanishes.

elastic strains (relative gaps being between 4 and 6% on average over the studied temperature profiles) but also provided estimates of stress evolution profiles during the process by using temperature-dependent elastic properties.

In addition, the analysis also reveals that computing temperature estimates only from synchrotron X-ray diffraction measurements is not trivial.

Finally, complex, large-scale processes such as DED or powder-bed fusion are almost impossible to model perfectly at part scale, and would therefore benefit from experimental studies in combination with the strategy proposed in this contribution, as numerical results are corrected using experimental data without increasing the level of modeling detail, hence maintaining short computation time, while allowing estimation of quantities of interest inaccessible to direct measurements, such as stress evolution during the process.

Declaration of competing interest The authors declare the following financial interests/personal relationships which may be considered as potential competing interests: Manas Upadhyay reports financial support was provided by European Research Council. If there are other authors, they declare that they have no known competing financial interests or personal relationships that could have appeared to influence the work reported in this paper.

CRediT authorship contribution statement S. Gaudez: Writing – review & editing, Writing – original draft, Investigation, Formal analysis, Data curation, Conceptualization. **D. Weisz-Patrault**: Writing – review & editing, Writing – original draft, Software, Methodology, Formal analysis, Conceptualization. **K.A. Abdesselam**: Validation, Methodology, Investigation. **H. Gharbi**: Methodology, Data curation. **V. Honkimäki**: Resources, Methodology, Conceptualization. **S. Van Petegem**: Writing – review & editing, Resources, Methodology, Conceptualization. **M.V. Upadhyay**: Writing – review & editing, Writing – original draft, Supervision, Methodology, Conceptualization, Project administration, Funding acquisition.

Acknowledgments The authors acknowledge the support of the European Synchrotron Radiation Facility (ESRF) for beamtime access via proposal no. ME-1578 and thank Florian Russello for assistance and support in using beamline ID31. The authors thank Simon Hallais for support in conducting EBSD measurements. SG, KAA and MVU are grateful to European Research Council (ERC) for their support through the European Union's Horizon 2020 research and innovation program for project GAMMA (Grant agreement ID: 946959).

Funding This work was supported by the Horizon 2020 - EXCELLENT SCIENCE - European Research Council Starting Grant 2020 project GAMMA (Grant agreement ID: 946959).

Data availability Data will be made available on request. Open access to synchrotron experimental raw data will be available on December 2024, see https://doi.org/10.15151/ESRF-ES-611485530

References

[1] T. DebRoy, H. L. Wei, J. S. Zuback, T. Mukherjee, J. W. Elmer, J. O. Milewski, A. M. Beese, A. Wilson-Heid, A. De, and W. Zhang, "Additive manufacturing of metallic components – Process, structure and properties," Progress in Materials Science, vol. 92, pp. 112–224, 2018.

[2] D. Svetlizky, M. Das, B. Zheng, A. L. Vyatskikh, S. Bose, A. Bandyopadhyay, J. M. Schoenung, E. J. Lavernia, and N. Eliaz, "Directed energy deposition (DED) additive manufacturing: Physical characteristics, defects, challenges and applications," Materials Today, vol. 49, pp. 271–295, 2021.

[3] C. S. Lough, X. Wang, C. C. Smith, R. G. Landers, D. A. Bristow, J. A. Drallmeier, B. Brown, and E. C. Kinzel, "Correlation of SWIR imaging with LPBF 304L stainless steel part properties," Additive Manufacturing, vol. 35, p. 101359, 2020.

[4] S. K. Everton, M. Hirsch, P. Stravroulakis, R. K. Leach, and A. T. Clare, "Review of in-situ process monitoring and in-situ metrology for metal additive manufacturing," Materials & Design, vol. 95, pp. 431–445, 2016.

[5] D. Weisz-Patrault, "Fast simulation of temperature and phase transitions in directed energy deposition additive manufacturing," Additive Manufacturing, vol. 31, p. 100990, 2020.

[6] W. Chen, L. Xu, Y. Han, L. Zhao, and H. Jing, "Control of residual stress in metal additive manufacturing by low-temperature solid-state phase transformation: An experimental and numerical study," Additive Manufacturing, vol. 42, p. 102016, 2021.

[7] D. Weisz-Patrault, P. Margerit, and A. Constantinescu, "Residual stresses in thin walled-structures manufactured by directed energy deposition: In-situ measurements, fast thermo-mechanical simulation and buckling," Additive Manufacturing, vol. 56, p. 102903, 2022.

[8] J. Jeong, S. Webster, S. Liao, J.-E. Mogonye, K. Ehmann, and J. Cao, "Cooling rate measurement in directed energy deposition using photodiode-based planck thermometry (pdpt)," Additive Manufacturing Letters, vol. 3, p. 100101, 2022.

[9] P. A. Hooper, "Melt pool temperature and cooling rates in laser powder bed fusion," Additive Manufacturing, vol. 22, pp. 548–559, 2018.

[10] T. Becker, S. J. Altenburg, N. Scheuschner, P. P. Breese, C. Metz, K. Hilgenberg, and C. Maierhofer, "In-situ monitoring of the laser powder bed fusion build process via bi-chromatic optical tomography," Procedia CIRP, vol. 111, pp. 340–344, 2022.

[11] F. Uzun, H. Basoalto, K. Liogas, J. Chen, I. P. Dolbnya, Z. I. Wang, and A. M. Korsunsky, "Voxel-based full-field eigenstrain reconstruction of residual stresses in additive manufacturing parts using height digital image correlation," Additive Manufacturing, vol. 77, p. 103822, 2023.

[12] C. Ioannidou, H.-H. König, N. Semjatov, U. Ackelid, P. Staron, C. Koerner, P. Hedström, and G. Lindwall, "In-situ synchrotron X-ray analysis of metal additive manufacturing: Current state, opportunities and challenges," Materials & Design, vol. 219, p. 110790, 2022.

[13] L. Wang, Q. Guo, L. Chen, and W. Yan, "In-situ experimental and high-fidelity modelling tools to advance understanding of metal additive manufacturing," International Journal of Machine Tools and Manufacture, p. 104077, 2023.

[14] W. Lu, L. Zhao, Z. Su, J. Li, and Q. Hu, "Recent progress on in-situ characterization of laser additive manufacturing process by synchrotron radiation," Journal of Materials Science & Technology, 2024.

[15] S. Hocine, H. Van Swygenhoven, S. Van Petegem, C. S. T. Chang, T. Maimaitiyili, G. Tinti, D. F. Sanchez, D. Grolimund, and N. Casati, "Operando X-ray diffraction during laser 3D printing," Materials Today, vol. 34, pp. 30–40, 2020.

[16] Y. Chen, S. J. Clark, D. M. Collins, S. Marussi, S. A. Hunt, D. M. Fenech, T. Connolley, R. C. Atwood, O. V. Magdysyuk, G. J. Baxter, et al., "Correlative synchrotron X-ray imaging and diffraction of directed energy deposition additive manufacturing," Acta Materialia, vol. 209, p. 116777, 2021.

[17] A. C. de F. Silveira, R. Fechte-Heinen, and J. Epp, "Microstructure evolution during laser-directed energy deposition of tool steel by in situ synchrotron X-ray diffraction," Additive Manufacturing, vol. 63, p. 103408, 2023.

[18] M. Chen, M. Simonelli, S. Van Petegem, Y. Yau Tse, C. Sin Ting Chang, M. Grazyna Makowska, D. Ferreira Sanchez, and H. Moens-Van Swygenhoven, "A quantitative study of thermal cycling along the build direction of Ti-6Al-4V produced by laser powder bed fusion," Materials & Design, vol. 225, p. 111458, 2023.

[19] H.-H. König, N. H. Pettersson, A. Durga, S. Van Petegem, D. Grolimund, A. C. Chuang, Q. Guo, L. Chen, C. Oikonomou, F. Zhang, et al., "Solidification modes during additive manufacturing of steel revealed by high-speed X-ray diffraction," Acta Materialia, vol. 246, p. 118713, 2023.

[20] P. Gh Ghanbari, P. Markovic, S. Van Petegem, M. G. Makowska, R. Wrobel, T. Mayer, C. Leinenbach, E. Mazza, and E. Hosseini, "A close look at temperature profiles during laser powder bed fusion using operando X-ray diffraction and finite element simulations," Additive Manufacturing Letters, vol. 6, p. 100150, 2023.

[21] S. A. Oh, R. E. Lim, J. W. Aroh, A. C. Chuang, B. J. Gould, B. Amin-Ahmadi, J. V. Bernier, T. Sun, P. C. Pistorius, R. M. Suter, et al., "High speed synchrotron X-ray diffraction experiments resolve microstructure and phase transformation in laser processed Ti-6Al-4V," Materials Research Letters, vol. 9, no. 10, pp. 429–436, 2021.

[22] S. A. Oh, R. E. Lim, J. W. Aroh, A. C. Chuang, B. J. Gould, J. V. Bernier, N. Parab, T. Sun, R. M. Suter, and A. D. Rollett, "Microscale observation via high-speed X-ray diffraction of alloy 718 during in situ laser melting," JOM, vol. 73, no. 1, pp. 212–222, 2021.

[23] F. Schmeiser, E. Krohmer, N. Schell, E. Uhlmann, and W. Reimers, "Internal stress evolution and subsurface phase transformation in titanium parts manufactured by laser powder bed fusion—an in situ X-ray diffraction study," Advanced Engineering Materials, vol. 23, no. 11, p. 2001502, 2021.

[24] S. A. Oh, J. W. Aroh, N. L. Lamprinakos, C. A. Chuang, A. N. Bucsek, and A. D. Rollett, "Martensite decomposition during rapid heating of Ti-6Al-4V studied via in situ synchrotron X-ray diffraction," Communications Materials, vol. 5, no. 1, p. 58, 2024.

[25] L. Gao, A. C. Chuang, P. Kenesei, Z. Ren, L. Balderson, and T. Sun, "An operando synchrotron study on the effect of wire melting state on solidification microstructures of Inconel 718 in wire-laser directed energy deposition," International Journal of Machine Tools and Manufacture, vol. 194, p. 104089, 2024.

[26] A. C. d. F. Silveira, L. T. Belkacemi, P. J. de Castro, M. Schowalter, R. Fechte-Heinen, and J. Epp, "Effect of intrinsic heat treatment on the precipitate formation of X40CrMoV5-1 tool steel during laser-directed energy deposition: a coupled study of atom probe tomography and in situ synchrotron X-ray diffraction," Acta Materialia, p. 120488, 2024.

[27] M. Chiumenti, M. Cervera, A. Salmi, C. A. De Saracibar, N. Dialami, and K. Matsui, "Finite element modeling of multi-pass welding and shaped metal deposition processes," Computer methods in applied mechanics and engineering, vol. 199, no. 37-40, pp. 2343–2359, 2010.

[28] G. Marion, G. Cailletaud, C. Colin, and M. Mazière, "A finite element model for the simulation of direct metal deposition," in International Congress on Applications of Lasers & Electro-Optics, vol. 1, pp. 834–841, LIA, 2014.

[29] E. R. Denlinger and P. Michaleris, "Effect of stress relaxation on distortion in additive manufacturing process modeling," Additive Manufacturing, vol. 12, pp. 51–59, 2016.

[30] J. Smith, W. Xiong, J. Cao, and W. K. Liu, "Thermodynamically consistent microstructure prediction of additively manufactured materials," Computational mechanics, vol. 57, no. 3, pp. 359–370, 2016.

[31] T. Keller, G. Lindwall, S. Ghosh, L. Ma, B. M. Lane, F. Zhang, U. R. Kattner, E. A. Lass, J. C. Heigel, Y. Idell, et al., "Application of finite element, phase-field, and calphad-based methods to additive manufacturing of ni-based superalloys," Acta materialia, vol. 139, pp. 244–253, 2017.

[32] Q. Chen, G. Guillemot, C.-A. Gandin, and M. Bellet, "Three-dimensional finite element thermomechanical modeling of additive manufacturing by selective laser melting for ceramic materials," Additive Manufacturing, vol. 16, pp. 124–137, 2017.

[33] M. Biegler, A. Marko, B. Graf, and M. Rethmeier, "Finite element analysis of in-situ distortion and bulging for an arbitrarily curved additive manufacturing directed energy deposition geometry," Additive Manufacturing, vol. 24, pp. 264–272, dec 2018.

[34] A. Edwards, D. Weisz-Patrault, and E. Charkaluk, "Analysis and fast modelling of microstructures in duplex stainless steel formed by directed energy deposition additive manufacturing," Additive Manufacturing, vol. 61, p. 103300, 2023.

[35] S. Gaudez, K. A. Abdesselam, H. Gharbi, Z. Hegedüs, U. Lienert, W. Pantleon, and M. V. Upadhyay, "High-resolution reciprocal space mapping reveals dislocation structure evolution during 3D printing," Additive Manufacturing, vol. 71, p. 103602, 2023.

[36] P. Withers, M. Preuss, A. Steuwer, and J. Pang, "Methods for obtaining the strain-free lattice parameter when using diffraction to determine residual stress," Journal of applied crystallography, vol. 40, no. 5, pp. 891–904, 2007.

[37] D. Bäuerle, Laser processing and chemistry. Springer Science & Business Media, 2013.

[38] CEA, "Cast3m," 2020. Commissariat à l'Énergie Atomique, http://www-cast3m.cea.fr/.

[39] "High temperature characteristics of stainless steels," tech. rep., A Designers' Handbook Series No. 9004. American Iron and Steel Institute, 2011.

[40] S. S. Lee, U.-S. Min, B. Ahn, and S. H. Yoo, "Elastic constants determination of thin cold-rolled stainless steels by dynamic elastic modulus measurements," Journal of materials science, vol. 33, no. 3, pp. 687–692, 1998.

[41] P. Margerit, D. Weisz-Patrault, K. Ravi-Chandar, and A. Constantinescu, "Tensile and ductile fracture properties of as-printed 316L stainless steel thin walls obtained by directed energy deposition," Additive Manufacturing, vol. 37, p. 101664, 2021.

[42] Y. Balit, E. Charkaluk, and A. Constantinescu, "Digital image correlation for microstructural analysis of deformation pattern in additively manufactured 316L thin walls," Additive Manufacturing, vol. 31, p. 100862, 2020.

[43] D. Weisz-Patrault, S. Sakout, and A. Ehrlacher, "Fast simulation of temperature and grain growth in directed energy deposition additive manufacturing," in 14th WCCM-ECCOMAS Congress, Scipedia, 2021.

[44] P. Mercelis and J.-P. Kruth, "Residual stresses in selective laser sintering and selective laser melting," Rapid prototyping journal, vol. 12, no. 5, pp. 254–265, 2006.

[45] N. Mohanan, J. G. S. Macías, J. Bleyer, T. Helfer, and M. V. Upadhyay, "Intergranular stress and plastic strain formation during laser scanning of additively manufactured stainless steel: An experimentally-driven thermomechanical simulation study," Materialia, p. 102082, 2024.

[46] F. Schmeiser, E. Krohmer, N. Schell, E. Uhlmann, and W. Reimers, "Experimental observation of stress formation during selective laser melting using in situ X-ray diffraction," Additive Manufacturing, vol. 32, p. 101028, 2020.

[47] T. Mukherjee, W. Zhang, and T. DebRoy, "An improved prediction of residual stresses and distortion in additive manufacturing," Computational Materials Science, vol. 126, pp. 360–372, 2017.

[48] A. Plotkowski, K. Saleeby, C. M. Fancher, J. Haley, G. Madireddy, K. An, R. Kannan, T. Feldhausen, Y. Lee, D. Yu, et al., "Operando neutron diffraction reveals mechanisms for controlled strain evolution in 3d printing," Nature Communications, vol. 14, no. 1, p. 4950, 2023.